Short communication: Synchrotron-based elemental mapping of single grains to investigate variable infrared-radiofluorescence emissions for luminescence dating

Mariana Sontag-González[1,2*], Raju Kumar[3*], Jean-Luc Schwenninger[3], Juergen Thieme[1,4], Sebastian Kreutzer[5], Marine Frouin[1]

[1] Department of Geosciences, Stony Brook University, 255 Earth and Space Sciences Building, Stony Brook, NY 11794-2100, USA
[2] Department of Geography, Justus Liebig University Giessen, 35390 Giessen, Germany
[3] Research Laboratory for Archaeology and the History of Art, University of Oxford, Dyson Perrins Building, South Parks Road, OX1 3QY, Oxford, UK
[4] Institute for X-Ray Physics, Georg-August-University of Goettingen, Germany
[5] Institute of Geography, Ruprecht-Karl University of Heidelberg, 69120 Heidelberg, Germany

*These authors contributed equally to this work.

Correspondence to: Mariana Sontag-González (mariana.sontag-gonzalez@geogr.uni-giessen.de) or Raju Kumar (raju.kumar@arch.ox.ac.uk)

Abstract. During ionizing irradiation, potassium (K)-rich feldspar grains emit infrared (IR) light, which is used for infrared-radiofluorescence (IR-RF) dating. The late-saturating IR-RF emission centred at ~880 nm represents a promising tool to date Quaternary sediments. In the present work, we report the presence of individual grains in the K-feldspar density fraction displaying an aberrant IR-RF signal shape, whose combined intensity contaminates the sum signal of an aliquot composed of dozens of grains. Our experiments were carried out at the National Synchrotron Light Source (NSLS-II) at the submicron resolution X-ray spectroscopy (SRX) beamline. We analysed coarse (> 90 µm) K-feldspar bearing grains of five samples of different ages and origin in order to characterize the composition of grains yielding the desired or contaminated IR-RF emission. Using micro-X-ray-fluorescence (µ-XRF), we successfully acquired element distribution maps of up to 15 elements (<1 µm resolution) of sections of full grains previously used for ~~luminescence~~ IR-RF dating. In keeping with current theories of IR-RF signal production, we observed a trend between the relative proportions of Pb and Fe and the shape of the IR-RF ~~luminescence~~ signal: most grains with the desired IR-RF signal shape had high Pb and low Fe contents. Interestingly, these grains were also defined by high Ba and low Ca contents. Our study also represents a proof-of-concept for mapping the oxidation states of Fe using micro-X-ray absorption near-edge structure spectroscopy (µ-XANES) on individual grains. The high spatial resolution enabled by synchrotron X-ray spectroscopy makes it a powerful tool for future experiments to elucidate long-standing issues concerning the nature and type of defect(s) associated with the main dosimetric trap in feldspar.

1 Introduction

Geochronologic data provide essential information for understanding the rates of Earth's surface processes, environmental changes, and the evolution of life. Advances in dating techniques have fundamentally changed our capacity to piece together our evolutionary past over millions of years, with luminescence dating proving to be a powerful tool in this field as it applies to various types of sediments and contexts. The technique determines an age estimate for when mineral grains were last exposed to daylight or heat. Luminescence dating methods rely on the property of certain minerals to record the amount of radiation to which they have been exposed during burial and release energy when exposed to sunlight or high temperature (e.g., Aitken, 1985, 1998; Bateman, 2019). In the laboratory, the total amount of energy per unit mass stored in the mineral is measured (dose, with the unit Gy). The energy absorption rate per unit mass (dose rate, with the unit Gy a^{-1}) is derived from knowledge of the natural radioactivity surrounding the sampled sediments. The quotient of these two values (dose/dose rate) gives the burial age.

Of the two minerals routinely used for luminescence dating of sediments, quartz and potassium (K-)-rich feldspar, the latter allows for the routine dating of older deposits of up to ~300 000 years or ~9600 000 years (considering a dose rate of 3 Gy ka^{-1} or 1 Gy ka^{-1}, respectively) using infrared stimulated luminescence (IRSL, Hütt et al., 1988). The datable upper age limit is given by the IRSL signal saturation after exposure to radiation doses around 9600 Gy (see summary in Sec. 8.1 in Murari et al., 2021a). Over the past decades, different methods have been proposed to extend this upper age limit with varying degrees of success. The infrared-radiofluorescence (IR-RF) signal of K-feldspar is a promising candidate for such an extension. The RF signal arises from prompt radiative recombination of charge within crystalline materials during continuous exposure to ionizing radiation. The IR-RF emission at 880 nm (e.g., Kumar et al., 2018; Riedesel et al., 2021; Sontag-González et al., 2022) decreases in intensity with dose accumulation as the electron traps fill until saturation (Trautmann et al., 1999a). This saturation level constrains the time range over which IR-RF dating is applicable.

Murari et al. (2018) demonstrated that an accurate dose recovery of a known dose of 3600 Gy is possible (a dose recovery test is a laboratory performance check of the measurement protocol, and successful dose recovery is a prerequisite for any protocol). If we assume typical environmental dose rates of between 3 Gy ka^{-1} and 1 Gy ka^{-1}, then IR-RF dating could produce age estimates ranging from 1.2 Ma to 3.6 Ma, which is around four times greater than the upper dating limit of conventional luminescence dating methods. However, more recent studies (Murari et al., 2021b; Kreutzer et al., 2022) indicated a dose saturation at around 1500 Gy, reducing the previously predictedassumed temporal limit of IR-RF dating. Hence, the uncertainty surrounding its upper age limit remains and further studies on known-age samples are required to assess whether the sample/grain geochemistry influences the age limit. There is undoubtedly a gap in our current understanding of the luminescence IR-RF production processes in K-feldspar, and a revised conceptual model might be needed.

The vast majority of IR-RF studies have been performed on multi-grain aliquots, so the possible effects of variability of the IR-RF signal (e.g., differences in signal saturation or in proportions of RF emissions) from different grains has not received much attention in the literature so far, as detailed in section 2. Here, we investigate the IR-RF signal of five samples

66 from different locations at single-grain resolution and discuss ~~what~~ the effect ~~that~~ the observed variability could have on multi-

67 grain aliquots. To assess whether the grain geochemistry influences the IR-RF signal and potentially the age limit of IR-RF,

68 we examined individual K-feldspar grains at the submicron resolution X-ray spectroscopy (SRX) beamline at the National

69 Synchrotron Light Source II (NSLS-II) at Brookhaven National Laboratory. Measurements at such a high-resolution may lead

70 to a better understanding of the luminescence kinetics in feldspars. We report on the feasibility and practicality of using μ-X-

71 ray fluorescence (μ-XRF) and μ-X-ray absorption near-edge fine structure (μ-XANES) techniques in investigating the

72 ~~luminescence~~ IR-RF signal origin and kinetics in K-feldspar.

2 Method and rationale

74 Identification of the defect type linked to the IR-RF signal and its concentration would enable us to better characterize the light

75 emission (signal sensitivity) in different types of feldspar, while identification of the origin of ~~possible contamination in the~~RF

76 emissions ~~IR-RF signal~~ could help us to gain a better understanding ~~of~~about the apparent ~~early~~ saturation or quenching of the

77 IR-RF signal. μ-XRF and μ-XANES produce high-resolution maps of elements and their oxidation states and are well suited

78 for the purposes of our study. μ-XRF elemental analyses are based on the characteristic fluorescence of atoms when stimulated

79 with X-rays with a higher energy than their ionization energy. In the case of μ-XANES, initial measurements of standards are

80 run by varying the incident beam energy to determine the specific energy equal to the absorption edge (binding energy of inner

81 shell electrons) of the element or ion of interest. This is apparent by an abrupt rise in the resulting fluorescence, which is

82 different between oxidation states as they require different minimum stimulation energies before ionization and subsequent

83 fluorescence. μ-XRF maps using the obtained absorption edge energies allow for maps of the different oxidation states of the

84 same element.

85 The use of synchrotron μ-XRF allows us to improve the spatial resolution compared with a standard lab-bench μ-

86 XRF setup (e.g., Buylaert et al., 2018) by reducing the beam spot size from ~25 μm to 1 μm or 0.5 μm. ~~Though B~~both the

87 grain geochemistry and crystallography should be investigated to characterize the defect type and its environment~~,~~. ~~i~~In the

88 present study, we focus~~sed~~ only on geochemistry, though our results should be complemented with crystallographic studies in

89 future work.

90 The defect(s) responsible for the IR-RF emissions are still subject to debate. It has been suggested that IR-RF occurs

91 as a result of the change in the oxidation state of the participating lead (Pb) defect via the transition: $Pb^{2+} \rightarrow (Pb^+)^* \rightarrow Pb^+$

92 (Nagli and Dyachenko, 1986; Erfurt, 2003). A similar transition has been suggested for amazonite (see Ostrooumov, 2016),

93 but the direct connection between the Pb-centre and IR-RF has not yet been evidenced. Other reactions involving higher

94 oxidation states~~Pb⁴⁺~~ would also be possible but have~~n't~~ not yet been observed or formally proposed. Additionally, the IR-RF

95 signal is composed of at least two separate emissions. Previous publications placed the main IR emission at 1.43 eV (865 nm)

96 based on Trautmann et al. (1999a, b) and Erfurt and Krbetschek (2003), but more recent work including corrections for the

97 spectrometer efficiency places the IR emission closer to 880 nm (Kumar et al., 2018; Riedesel et al., 2021; Sontag-González

et al., 2022). A second IR emission centred at 955 nm (1.30 eV) at lower intensity has also been identified (Kumar et al., 2018), which partly overlaps with the 880 nm peak.

The presence of iron (Fe) in feldspar is known to lead to red RF (e.g., Telfer and Walker, 1978; Brooks et al., 2002; Visocekas et al., 2014), with the maximum peak wavelength varying between 700 nm and 770 nm depending on feldspar composition (Dütsch and Krbetschek, 1997; Krbetschek et al., 2002). Such observations are in line with the suggestion of more than one component in the red photoluminescence of K-feldspar (Prasad and Jain, 2018). Despite the occurrence of the red RF emission in Fe^{3+} state, its initial state remains a subject of many debates, with conflicting opinions suggesting either Fe^{2+} (Fe^{2+} + h → Fe^{3+}; here h stands for hole) or Fe^{4+} (Fe^{4+} + e^- → Fe^{3+}; here e^- stands for electron) (Kirsh and Townsend, 1988; Jain et al., 2015). Recently, Kumar et al. (2020) argued that the initial state must be Fe^{4+} based on their findings using cathodoluminescence microscopy. Spectral analyses showed that, with dose exposure, the red RF emission (~710 nm emission in K-feldspar) increases, while the 880 nm emission decreases (Krbetschek et al., 2000; Erfurt and Krbetschek, 2003; Kumar et al., 2018; Frouin et al., 2019). The thermal stability of the ~710 nm emission has been, however, questioned (e.g., Krbetschek et al., 2000). Such a reduced thermal stability might be an issue for IR-RF dating, as it has been suggested that the tail of the ~710 nm emission overlaps with the 880 nm emission, thus potentially playing a role in the shape of the measured IR-RF. Such a contribution can be reduced to less than 5% of the IR-RF signal by using a bandpass filter centred at 850 nm (FWHM 40 nm), but can still affect the equivalent dose (D_e) value at doses near signal saturation (see Sontag-González and Fuchs, 2022). D_e values are determined by sliding the IR-RF dose-response curve of grains containing the natural signal onto that obtained after a full bleach of the same aliquot. In summary, although previous studies have identified factors that may influence the IR-RF signal in several ways, e.g., whether the IR-RF signal originates from Pb, and is affected by the presence of Fe^{2+} or Fe^{4+}, a conclusive confirmation or comprehensive linkage between these factors is yet to be established.

A possible variability of the several RF emissions in individual grains has received scant attention, so far. Trautmann et al. (2000) were the first to analyse the IR-RF signal of individual K-feldspar grains. Using spectral measurements of 21 to 42 grains from three samples, they observed up to four emissions (IR, red, yellow, blue) with variable intensities (a fourth sample appears in their figure 3 but is not mentioned in the main text). An IR-RF dose-response curve was only reported for one grain, which had a similar shape, albeit a later onset of saturation, when compared to the response from the multi-grain aliquot of the same sample. More recently, Mittelstraß and Kreutzer (2021) analysed 60 grains from two samples, of which 55% and 80% emitted a detectable signal. In that study, between one and three grains per sample (~9% of signal-emitting grains for both samples) were rejected due to a bad match between the natural and regenerative curves, which might have been caused by equipment issues, but also due to sensitivity changes (Varma et al., 2013). However, all grains that emitted a detectable signal displayed the expected decay shape for IR-RF (decreasing signal with increasing dose). Likewise, own laboratory observations indicated that the signal varies in sensitivity across feldspar minerals and can be contaminated for various reasons, leading to spectral interference or quenching, ultimately influencing the saturation level and/or the shape of the IR-RF signal (Frouin et al., 2017, 2019; Kumar et al., 2020).

To investigate these issues, first, we recorded IR-RF curves from individual grains in our luminescence dating laboratory at the Research Laboratory for Archaeology and the History of Art (RLAHA) at the University of Oxford (UK). Then, during our beam time (96 h), and as a proof of concept, we optimized the measurement conditions and obtained compositional maps of the individual K-feldspar grains. We paid particular attention to K, Ca, Fe and Pb. After analysing the μ-XRF maps, μ-XANES measurements were done at selective spots where Fe ~~and Pb~~ occurred in greater concentrations. Note: The atomic number of sodium (Na; another end member of the feldspar ternary system) is too low to be measured at the current SRX beamline.

3 Material and instrumentation

A total of five samples were selected to represent a diversity of i) geological context, ii) geochemistry, iii) shape of the IR-RF signal, and iv) age. Sample Gi326 from a Triassic sandstone from Bayreuth, Germany, is composed of 89% of K-feldspar (Sontag-González and Fuchs, 2022) and has previously been used as a reference sample in a laboratory comparison of IR-RF dating (Murari et al., 2021b). X7343 was collected from a Pliocene sediment at the Nyayanga site in the Homa peninsula, Kenya (Plummer et al., 2023). X7363 was taken from the Gele Tuff in the Turkana Basin, Kenya, ~~and~~ dated by Ar/Ar at 1.315~~2~~ ± 0.00~~2~~ Ma (Phillips et al., 2023). Previous compositional analyses of Gele Tuff pumice feldspars (crushed clasts without density separation) indicate they are mostly composed of anorthoclase with smaller proportions of sanidine and plagioclase; K, Na and Ca contents ranged ~1–6 wt %, ~5–6 wt % and ~0–3 wt %, respectively, without appreciable differences between the grains' cores and rims (Phillips et al., 2023). Relatively high Ba contents of up to 0.8wt% were also reported in that study, with a positive correlation between Ba and Na contents. X7368 is a sediment sample collected above the Silbo Tuff (0.751 ± 0.022 Ma, McDougall and Brown, 2006) and below the Kale Tuff (younger than the Silbo Tuff but not directly dated) in the Turkana Basin, Kenya. Sample H22550 is a coastal marine sample from Sula, Russia, dated by quartz single-aliquot-regenerative optically stimulated luminescence (OSL) at 103 ± 8 ka (Murray et al., 2007) and was used in the past as a reference sample to test the accuracy of IR-RF dating (Buylaert et al., 2012). All samples were prepared following conventional treatments (e.g., Preusser et al., 2008), including wet-sieving to isolate the desired grain size fraction, chemical treatment with HCl at 10% to remove carbonates and H_2O_2 at 30% for a few hours to a few days to remove organic matter, and density separation at 2.58 g cm^{-3} using a heavy liquid solution to enrich K-feldspar grains. Sample H22550 was then etched with diluted HF (10%, 40 min). All grains were exposed under a solar simulator SOL Hönle 2 for a few days to reset their signal.

Unmeasured grains of sample X7343 were placed on a stub mount on a piece of carbon tape, then imaged with a scanning electron microscope (SEM) equipped for energy-dispersive X-ray spectroscopy (EDS) at Archéosciences Bordeaux (FR) (JEOL JSM-6460LV; detector: Oxford Instruments X-Max (51-XMX0002); software: Oxford Instruments INCA version 4.11). The SEM was operated at 20 kV and 55 μA beam current. Sample X7343 is referred to as BDX22338 in the Archéosciences Bordeaux system.

162   IR-RF measurements were recorded with a *lexsyg research* luminescence reader fitted with an annular $^{90}Sr/^{90}Y$ beta

163   source (Richter et al., 2013) using a bandpass filter centred at 850 nm (FWHM 40 nm) mounted in front of a Hamamatsu

164   H7421-50 photo-multiplier tube. Measurements were performed at 70°C, following Frouin et al. (2017). Multi-grains and

165   single-grains were measured on stainless steel cups. High-resolution compositional analysis of the grains was undertaken at

166   the SRX beamline at NSLS-II (Chen-Wiegart et al., 2016). After IR-RF measurements, the grains were removed from the

167   stainless steel cups and fixed on a polymer microscope slide (UVT acrylic; Agar Scientific) with a small piece of carbon tape

168   to avoid misplacement during measurement (supplementary Fig. S1). μ-XRF maps were obtained by scanning across pre-

169   selected regions on the grains with low topographic changes (90 x 90 μm maps, with a step size of 0.67 μm and an integration

170   time of 0.1 s). The incident X-ray beam was focussed by a pair of Kirkpatrick-Baez mirrors. An incident beam energy of 13.5

171   keV was used for the μ-XRF measurements. The excited elements' characteristic fluorescence was obtained from the sum of

172   the four elements of a silicon drift detector. All μ-XRF measurements were normalized to the corresponding incident X-ray

173   flux (I_0) (supplementary Fig. S2).

174   The μ-XANES maps cover 60 x 60 μm in steps of 0.5 μm, thus creating a grid with 120 x 120 data points (i.e., 14

175   400 μ-XRF spectra). To obtain ~~μ-XANES~~ maps of Fe-states in our samples, we varied the incident beam energy according to

176   the absorption edge values obtained from the μ-XANES spectral measurements of Fe standards (Fe foil, pyrite, hematite). The

177   μ-XANES maps were measured three times to obtain μ-XRF emission spectra restricting the Fe species to either (i) the total

178   Fe (at 7.275 keV), (ii) the sum of Fe^{3+} and Fe^{2+} (at 7.134 keV), and (iii) only from Fe^{2+} (at 7.122 keV). The difference between

179   the intensity levels of the latter two measurements can qualitatively give the intensity levels of Fe^{3+}, i.e., $I_{Fe2+ \& Fe3+} - I_{Fe2+} =$

180   I_{Fe3+} where I (a.u.) refers to intensity, thus, the μ-XANES map of Fe^{3+}. We also attempted to record Pb states, however, the Pb

181   standard available at the SRX beamline was fully oxidized, which hindered establishing the correct beam energy for mapping.

182   Therefore, no Pb oxidation state maps were possible. μ-XRF and μ-XANES data were analysed using the open-source software

183   PyXRF v1.0.23 (Li et al., 2017) and ATHENA v0.9.26 (Ravel and Newville, 2005), respectively. Maps and plots were created

184   using **R** (R Core Team, 2022).

185   **4 Results**

186   **4.1 Multi-grain IR-RF signal**

187   The IR-RF signal of a multi-grain aliquot of 8 mm diameter of sample X7343 was first measured. The aliquot contained

188   hundreds of grains. The expected IR-RF signal of K-feldspar grains is a decaying function, e.g., a stretched single-exponential

189   (Erfurt et al., 2003). For sample X7343, however, we observed an unexpected shape of the IR-RF, consisting of a signal

190   decrease until 500 Gy succeeded by an increase, roughly following a saturating exponential shape that keeps increasing beyond

191   ~3800 Gy. The regenerative signal for one representative aliquot is shown in figure 1 (top right). We hypothesized that the

192   unexpected signal increase originates from a different source, potentially from a coating around the grains due to the

193   observation of a pinkish/reddish hue on some grains. Clay, Fe-oxide or other grain coatings are a common occurrence and

additional preparation steps are sometimes undertaken to remove them prior to luminescence measurements (e.g., Jayangondaperumal et al., 2012; Lomax et al., 2007; Rasmussen et al., 2023). We attempted to remove this signal contamination, using different chemical treatments such as HF, regal water, and heated regal water, however, without success. This suggests the signal is not originating from a coating. Therefore, we decided to investigate the mineral composition of sample X7343, using SEM-EDS on 118 randomly selected grains. Despite using density separation to isolate K-feldspar grains during chemical pre-treatment, we found that this sample was mainly composed of low-K grains (Fig. 1; top left). Indeed, over half of the grains had K-contents less than 2% and less than 5% of the grains had K-contents above 11%. The remainder exhibited K-contents between 2% and 10%. Note that a K-feldspar end member is 14% K (e.g., Gupta, 2015). The low-K grains, which correspond to the majority of grains, also had high Fe-contents of ~10%.

We then tested whether it was possible to isolate the desired decreasing IR-RF signal by handpicking grains based on their visual appearance under a microscope. Between 10 to 30 grains were placed onto two aliquots, one for transparent shiny angular grains and one for white-pinkish rounded grains. The regenerated IR-RF signals showed a clear distinction between the two aliquots (Fig. 1), proving it is possible to separate the two observed IR-RF shapes.

By manually selecting the grains based on their shape and colour and the subsequent multi-grain IR-RF measurements, we made three important observations: i) The decreasing IR-RF signal originates from a small number of grains (less than 5%), presumed to be K-feldspar. ii) The IR-RF signal of these grains decreased beyond 3800 Gy without reaching a plateau, indicating that a dose could be estimated beyond that value. iii) The increasing IR-RF signal originates from a different subset of grains, presumed to be the low-K, Fe-rich minerals identified via SEM-EDS.

4.2 Single-grain IR-RF characterisation

To further investigate this phenomenon, we measured the IR-RF signal of 22 individual grains from five samples of different origins (between one to eight grains per sample, Table 1). Each grain was manually placed on a sample holder (cup) and their signal was recorded over a 3,265 Gy beta irradiation. For each grain, their IR-RF signal shape falls into three categories (Fig. 2): Category #1 for grains with a decreasing IR-RF signal, category #2 for grains with an increasing IR-RF signal, and category #3 for grains with a flat signal. Within categories #1 and #2, the saturation level of the individual grains varies (Fig. 2b, d).

Among the five samples, one is a tuff, and two are originated from nearby volcanic environments and might, thus, be expected to yield abnormal luminescence behaviour. Common issues with volcanic samples are dim signals, different proportions of emissions, high fading rates and complex grain mineralogy (e.g., Krbetschek et al., 1997; Guérin and Visocekas, 2015; Joordens et al., 2015; Sontag-González et al., 2021; O'Gorman et al., 2021). However, we also observed the unwanted increasing IR-RF signal for one of the four grains for sample H22550, which is from a coastal sand deposit. The significance of this find is illustrated in figure 3, where curves representing the signals of individual grains from categories #1 and #2 were added together to simulate a multi-grain aliquot. We used the curves obtained from fitting a single stretched exponential decay function to the normalized data of one grain of sample X7343 (category #2) and one of Gi326 (category #1), since no category #1 grain was measured for sample X7343. When the total signal of the theoretical aliquot was composed of more than 50% of

227 signal from the category #2 grain, we observed the same decay shape as in figure 1 for a multi-grain aliquot of sample X7343.

228 Importantly, a synthetic mixture containing 20% of grains from category #2 still displayed the decaying shape characteristic

229 of category #1 grains. However, the curvature of its dose-response curve was altered, i.e., saturating earlier than the 'pure'

230 grain. Possible differences in long-term signal stability between the two grain categories could cause differences between the

231 summed curves of natural and regenerated IR-RF signals and thus lead to inaccurate equivalent doses for these mixtures.

232 Further, our results demonstrate that a satisfying IR-RF signal can be measured for all our samples, but only by

233 selecting grains with the appropriate ~~luminescence~~ IR-RF characteristics (presumably K-feldspar grains). We hypothesize that

234 the low-K grains with high Fe-content are the source of a contaminant IR-RF emission, which if not removed might result in

235 a wrong equivalent dose estimation (i.e., a wrong age estimate).

4.3 Sub-single grain μ-XRF elemental maps

237 Utilising μ-XRF, we identified up to 15 elements in the grains (see supplementary figure 3 for the total μ-XRF spectra). We

238 then fitted each of the spectra in the 135 by 135 pixel grid (i.e., 18 225 spectra) for each grain to obtain maps describing the

239 XRF intensity of each identified element. These maps only serve as qualitative indicators for the presence of elements and are

240 not corrected for the element-specific emission intensity or the energy-dependent efficiency of the detectors. For two grains,

241 we recorded additional μ-XRF maps to characterize visible inclusions (see table 1).

242 First, we consider only the presence/absence of each element with the IR-RF signals previously obtained. Most grains

243 across all categories contain K, Pb, and Fe, among other elements. Among the grains displaying a decreasing IR-RF signal

244 (category #1), all contain ~~K, Pb, Fe and~~ Ba~~, among other elements~~ (Fig. 4, middle), which is less present in grains from

245 categories #2 and #3. ~~Most of the grains from categories #2 and #3 also contain K, Pb and Fe, but few contain Ba.~~ Further,

246 most grains from categories #2 and #3 contain Ca, Ti and Mn, which are rare in the grains from category #1. The μ-XRF

247 intensities also allow for a qualitative comparison of elemental composition. As shown in the boxplots in figure 4 (right-hand

248 side), category #1 grains differ from those in category #2 and #3 primarily by a higher μ-XRF signal contribution from K and

249 a lower contribution from Fe.

250 If we compare the relative intensities of Pb, Fe and K, we can identify a pattern in the composition of grains from

251 each category (Fig. 5). Grains from category #1 tend to have high proportions of K and Pb and medium-to-low proportions of

252 Fe. All grains from categories #2 and #3 have medium-to-high proportions of Fe, and most have low levels of K and Pb. No

253 grains from categories #2 or #3 have high levels of both K and Pb. The element that distinguishes grains from categories #2

254 and #3 is Ca, which is only present in category #2 grains to a high proportion (see also supplementary figure 3).

255 Interestingly, the grains from category #3 cluster relatively close to those from category #2, suggesting that the

256 elemental composition alone is not responsible for the lack of IR-RF signal but that the spatial configuration of the elements

257 is another important factor to consider. This is exemplified in figure 6, which contains elemental maps of K, Pb and Fe for one

258 grain of each category. The category #1 grain (top row) tends to have K and Pb co-localized (overlap shown in green), whereas

259 the category #3 grain (bottom row) also contains both elements, but they appear in separate locations (shown in cyan and

yellow). In this grain, K appears co-localized with Fe (overlap shown in dark blue). Our preliminary observations require broader confirmation, but they are in line with the current hypotheses of emission origins for the K-feldspar IR-RF signal decreasing with dose (due to Pb) and a contaminating red RF signal increasing with dose (due to Fe). Furthermore, the lack of an IR-RF signal in category #3 grains appears to stem from low levels of K co-existing with high proportions of Fe, supporting the observations made by Kumar et al. (2020).

4.4 Mapping oxidation states with μ-XANES

By analysing absorption of X-rays near the absorption edge, μ-XANES spectra can provide information on the presence of potential oxidation states of an element, as shown in figure 7 through measurements of different standards of Fe; an increase in the oxidation state is generally accompanied by a shift in the absorption edge to higher energy (Fig. 7, inset).

We targeted the Fe-rich region of a category #1 grain (X7368) for mapping (location shown by the blue square in figure 6). Figure 8 shows the μ-XANES maps of three oxidation states (Fe^{3+} and Fe^{2+} combined, Fe^{2+}, and Fe^{3+}), all normalized to the maximum intensity level of the total Fe map. These maps suggest that Fe exists in the top section of this feldspar grain in its Fe^{3+} and Fe^{2+} states. Note how Fe^{2+} is mainly clustered in one region, possibly within a mineral inclusion with a rim of Fe^{3+}.

5 Conclusions and future work

We demonstrated that individual K-feldspar grains of the same five samples display different IR-RF behaviour, illustrated by different signal decay shapes (i.e., increasing or decreasing with dose and different saturation levels). These behaviours are cumulative (see figure 1), and therefore, the IR-RF signal of a multi-grain aliquot can lead to inaccurate equivalent doses. Despite the use of chemical preparations to remove contaminants, manually picking individual grains was necessary to isolate K-feldspar grains, which is unrealistic for routine dating applications in a low-light laboratory. A more realistic way to remove such contamination is by selecting K-feldspar grain populations by isolating the emission signal of individual grains with an imaging system. Here, we wanted to gain a further understanding of the production and origin of the emission signal, which ultimately will help us design a more appropriate imaging system for IR-RF dating. For sample X7343, we show through SEM-EDS analyses that the different emissions can be linked to different grain mineralogy. Since K-feldspar grains are known to be heterogeneous on a subgrain level, we propose synchrotron-based X-ray spectroscopy to characterize the grains on a submicron scale and investigate the origin of the IR-RF and other linked emissions. Information on the oxidation states of, e.g., Fe possibly allows for the characterisation of the reactions behind the electronic changes leading to radiofluorescence.

In the preliminary work presented here, we successfully applied μ-XRF and μ-XANES at the SRX beamline (NSLS-II) to obtain element and oxidation state maps of regions of interest within individual K-feldspar coarse grains previously used for IR-RF measurements. We were able to correlate the desired IR-RF signal shape (category #1) with compositions of high proportions of K, Pb, and Ba and low proportions of Fe. High proportions of Fe in the μ-XRF spectra were found in grains of

291 categories #2 and #3, but the possible role of Fe as a contaminant remains unclear. During our next beam time, we will polish
292 the grains down to a uniform surface prior to µ-XRF and µ-XANES measurements to limit surface effects. Such a setup will
293 also allow us to directly test the hypothesis that the contaminating IR-RF signal is coming from an element present at the
294 surface of the grain (e.g., iron coating possibly due to weathering), but not within the grain.

295 The relation between the chemical composition, crystal structure, and the shape of the IR-RF signal in individual K-
296 feldspar grains is still poorly understood, and efforts should be made to identify and quantify at high resolution the element
297 responsible for producing the IR-RF signal with the highest dynamic range (i.e., saturation at high dose). Our future work will
298 include implementing a second detector to simultaneously measure µ-XRF/µ-XANES and the IR-RF signal induced by the X-
299 rays. Though not widely used, X-rays are a suitable alternative to radioactive sources for luminescence dosimetry including
300 RF. The dual detection will allow us to isolate emissions from different mineral inclusions and directly correlate them to the
301 elemental composition, thereby assessing the extent of overlap of the desired IR-RF emission centred at 880 nm and
302 contaminating ones such as the possible unstable red emission associated with Fe^{3+}.

Data availability

304 The SEM dataset and the original data used to produce µ-XRF maps are available online (Sontag-González et al., 2023).

Author contribution

306 MF, JT, RK and JLS designed the experiments and prepared the samples. RK, JLS, and MF carried out the IR-RF
307 measurements. SK organized and analysed the SEM EDS measurements. MF and JT carried out the µ-XRF and µ-XANES
308 measurements. RK, MSG and MF analysed the results. MSG and RK prepared the manuscript with contributions from all
309 authors. MF, JT and JLS obtained funding.

Competing interests

311 The authors declare that they have no conflict of interest.

Acknowledgements

313 We are grateful to Svenja Riedesel and an anonymous referee for very constructive comments on an earlier version of this
314 manuscript. We thank Yannick Lefrais for operating the EDS at Archéosciences Bordeaux (former IRAMAT-CRP2A) in 2018.
315 This research used the SRX beamline of the National Synchrotron Light Source II, a U.S. Department of Energy (DOE) Office

316   of Science User Facility operated for the DOE Office of Science by Brookhaven National Laboratory under Contract No. DE-

317   SC0012704.

Financial support

319   This work was supported by the Natural Environment Research Council (grant number NE/T001313/1); and a Stony Brook

320   University-Brookhaven National Laboratory Seed Grant (#94508). The SEM analysis at Archéosciences Bordeaux was

321   supported by the Agence Nationale de la Recherche (grant no. ANR-10-LABX-52).

References

323   Aitken, M. J.: Thermoluminescence dating, Academic Press, London, 359 pp., 1985.

324   Aitken, M. J.: An introduction to optical dating: the dating of Quaternary sediments by the use of photon-stimulated

325   luminescence, Oxford University Press, Oxford, 267 pp., 1998.

326   Bateman, M. D.: Handbook of luminescence dating, edited by: Bateman, M. D., Whittles Publishing, Dunbeath, 400 pp.,

327   2019.

328   Brooks, R. J., Finch, A. A., Hole, D. E., Townsend, P. D., and Wu, Z.-L.: The red to near-infrared luminescence in alkali

329   feldspar, Contrib. Mineral. Petrol., 143, 484–494, https://doi.org/10.1007/s00410-002-0359-4, 2002.

330   Buylaert, J.-P., Jain, M., Murray, A. S., Thomsen, K. J., and Lapp, T.: IR-RF dating of sand-sized K-feldspar extracts: A test

331   of accuracy, Radiat. Meas., 47, 759–765, https://doi.org/10.1016/j.radmeas.2012.06.021, 2012.

332   Buylaert, J.-P., Újvári, G., Murray, A. S., Smedley, R. K., and Kook, M.: On the relationship between K concentration, grain

333   size and dose in feldspar, Radiat. Meas., 120, 181–187, https://doi.org/10.1016/j.radmeas.2018.06.003, 2018.

334   Chen-Wiegart, Y. K., Williams, G., Zhao, C., Jiang, H., Li, L., Demkowicz, M., Seita, M., Short, M., Ferry, S., Wada, T.,

335   Kato, H., Chou, K. W., Petrash, S., Catalano, J., Yao, Y., Murphy, A., Zumbulyadis, N., Centeno, S. A., Dybowski, C., and

336   Thieme, J.: Early science commissioning results of the sub-micron resolution X-ray spectroscopy beamline (SRX) in the

337   field of materials science and engineering, AIP Conference Proceedings, 1764, 030004, https://doi.org/10.1063/1.4961138,

338   2016.

339   Dütsch, C. and Krbetschek, M. R.: New methods for a better internal 40K dose rate determination, Radiat. Meas., 27, 377–

340   381, https://doi.org/10.1016/S1350-4487(96)00153-9, 1997.

341   Erfurt, G.: Infrared luminescence of Pb+ centres in potassium-rich feldspars, Phys. Status Solidi A, 200, 429–438,

342   https://doi.org/10.1002/pssa.200306700, 2003.

343   Erfurt, G. and Krbetschek, M. R.: Studies on the physics of the infrared radioluminescence of potassium feldspar and on the

344   methodology of its application to sediment dating, Radiat. Meas., 37, 505–510, https://doi.org/10.1016/S1350-

345   4487(03)00058-1, 2003.

346   Erfurt, G., Krbetschek, M. R., Bortolot, V. J., and Preusser, F.: A fully automated multi-spectral radioluminescence reading

347   system for geochronometry and dosimetry, Nucl. Instrum. Methods Phys. Res. Sect. B Beam Interact. Mater. At., 207, 487–

348   499, https://doi.org/10.1016/S0168-583X(03)01121-2, 2003.

349   Frouin, M., Huot, S., Kreutzer, S., Lahaye, C., Lamothe, M., Philippe, A., and Mercier, N.: An improved radiofluorescence

350   single-aliquot regenerative dose protocol for K-feldspars, Quat. Geochronol., 38, 13–24,

351   https://doi.org/10.1016/j.quageo.2016.11.004, 2017.

352   Frouin, M., Kumar, R., Kook, M, Buylaert, J.-P., Jain, M . Further investigation on IRRF and IRPL, 29/10/2019, DLED

353   conference, 2019.

354   Guérin, G. and Visocekas, R.: Volcanic feldspars anomalous fading: Evidence for two different mechanisms, Radiat. Meas.,

355   81, 218–223, https://doi.org/10.1016/j.radmeas.2015.08.009, 2015.

356   Gupta, A. K.: Origin of Potassium-rich Silica-deficient Igneous Rocks, Springer India, New Delhi,

357   https://doi.org/10.1007/978-81-322-2083-1, 2015.

358   Hütt, G., Jaek, I., and Tchonka, J.: Optical dating: K-Feldspars optical response stimulation spectra, Quat. Sci. Rev., 7, 381–

359   385, https://doi.org/10.1016/0277-3791(88)90033-9, 1988.

360   Jain, M., Sohbati, R., Guralnik, B., Murray, A. S., Kook, M., Lapp, T., Prasad, A. K., Thomsen, K. J., and Buylaert, J. P.:

361   Kinetics of infrared stimulated luminescence from feldspars, Radiat. Meas., 81, 242–250,

362   https://doi.org/10.1016/j.radmeas.2015.02.006, 2015.

363   Jayangondaperumal, R., Murari, M. K., Sivasubramanian, P., Chandrasekar, N., and Singhvi, A. K.: Luminescence dating of

364   fluvial and coastal red sediments in the SE Coast, India, and implications for paleoenvironmental changes and dune

365   reddening, Quat. Res., 77, 468–481, https://doi.org/10.1016/j.yqres.2012.01.010, 2012.

366   Joordens, J. C. A., d'Errico, F., Wesselingh, F. P., Munro, S., de Vos, J., Wallinga, J., Ankjærgaard, C., Reimann, T.,

367   Wijbrans, J. R., Kuiper, K. F., Mücher, H. J., Coqueugniot, H., Prié, V., Joosten, I., van Os, B., Schulp, A. S., Panuel, M.,

368   van der Haas, V., Lustenhouwer, W., Reijmer, J. J. G., and Roebroeks, W.: Homo erectus at Trinil on Java used shells for

369   tool production and engraving, Nature, 518, 228–231, https://doi.org/10.1038/nature13962, 2015.

370   Kirsh, Y. and Townsend, P. D.: Speculations on the blue and red bands in the TL emission spectrum of albite and

371   microcline, Int. J. Rad. Appl. Instrum. Part D. Nucl. Tracks Rad. Meas., 14, 43–49, https://doi.org/10.1016/1359-

372   0189(88)90040-4, 1988.

373   Krbetschek, M. R., Götze, J., Dietrich, A., and Trautmann, T.: Spectral information from minerals relevant for luminescence

374   dating, Radiat. Meas., 27, 695–748, https://doi.org/10.1016/S1350-4487(97)00223-0, 1997.

375   Krbetschek, M. R., Trautmann, T., Dietrich, A., and Stolz, W.: Radioluminescence dating of sediments: methodological

376   aspects, Radiat. Meas., 32, 493–498, https://doi.org/10.1016/S1350-4487(00)00122-0, 2000.

377   Krbetschek, M. R., Götze, J., Irmer, G., Rieser, U., and Trautmann, T.: The red luminescence emission of feldspar and its

378   wavelength dependence on K, Na, Ca – composition, Mineral. Petrol., 76, 167–177, https://doi.org/10.1007/s007100200039,

379   2002.

380   Kreutzer, S., Mercier, N., and Lamothe, M.: Infrared-radiofluorescence: Dose saturation and long-term signal stability of a

381   K-feldspar sample, Radiat. Meas., 156, 106818, https://doi.org/10.1016/j.radmeas.2022.106818, 2022.

382   Kumar, R., Kook, M., Murray, A. S., and Jain, M.: Towards direct measurement of electrons in metastable states in K-

383   feldspar: Do infrared-photoluminescence and radioluminescence probe the same trap?, Radiat. Meas., 120, 7–13,

384   https://doi.org/10.1016/j.radmeas.2018.06.018, 2018.

385   Kumar, R., Martin, L. I. D. J., Poelman, D., Vandenberghe, D., De Grave, J., Kook, M., and Jain, M.. Site-selective mapping

386   of metastable states using electron-beam induced luminescence microscopy, Sci. Rep., 10, 15650, 2020.

387   Li, L., Yan, H., Xu, W., Yu, D., Heroux, A., Lee, W.-K., Campbell, S. I., and Chu, Y. S.: PyXRF: Python-based X-ray

388   fluorescence analysis package, in: X-Ray Nanoimaging: Instruments and Methods III, 38–45,

389   https://doi.org/10.1117/12.2272585, 2017.

390   Lomax, J., Hilgers, A., Twidale, C. R., Bourne, J. A., and Radtke, U.: Treatment of broad palaeodose distributions in OSL

391   dating of dune sands from the western Murray Basin, South Australia, Quat. Geochronol., 2, 51–56,

392   https://doi.org/10.1016/j.quageo.2006.05.015, 2007.

393   Mittelstraß, D. and Kreutzer, S.: Spatially resolved infrared radiofluorescence: single-grain K-feldspar dating using CCD

394   imaging, Geochronology, 3, 299–319, https://doi.org/10.5194/gchron-3-299-2021, 2021.

395   McDougall, I. and Brown, F. H.: Precise 40Ar/39Ar geochronology for the upper Koobi Fora Formation, Turkana Basin,

396   northern Kenya, Journal of the Geological Society, 163, 205–220, https://doi.org/10.1144/0016-764904-166, 2006.

397   Murari, M. K., Kreutzer, S., and Fuchs, M.: Further investigations on IR-RF: Dose recovery and correction, Radiat. Meas.,

398   120, 110–119, https://doi.org/10.1016/j.radmeas.2018.04.017, 2018.

399   Murari, M. K., Kreutzer, S., King, G. E., Frouin, M., Tsukamoto, S., Schmidt, C., Lauer, T., Klasen, N., Richter, D.,

400   Friedrich, J., Mercier, N., and Fuchs, M.: Infrared radiofluorescence (IR-RF) dating: A review, Quat. Geochronol., 64,

401   101155, https://doi.org/10.1016/j.quageo.2021.101155, 2021a.

402   Murari, M. K., Kreutzer, S., Frouin, M., Friedrich, J., Lauer, T., Klasen, N., Schmidt, C., Tsukamoto, S., Richter, D.,

403   Mercier, N., and Fuchs, M.: Infrared Radiofluorescence (IR-RF) of K-Feldspar: An Interlaboratory Comparison,

404   Geochronometria, 48, 95–110, https://doi.org/10.2478/geochr-2021-0007, 2021b.

405   Murray, A. S., Svendsen, J. I., Mangerud, J., and Astakhov, V. I.: Testing the accuracy of quartz OSL dating using a known-

406   age Eemian site on the river Sula, northern Russia, Quat. Geochronol., 2, 102–109,

407   https://doi.org/10.1016/j.quageo.2006.04.004, 2007.

408   Nagli, L. E. and Dyachenko, S. V.: Luminescence of Pb+ ions in KCl:Pb crystals, Opt. Spectrosc., 61, 91–94, 1986.

409   O'Gorman, K., Tanner, D., Sontag-González, M., Li, B., Brink, F., Jones, B. G., Dosseto, A., Jatmiko, Roberts, R. G., and

410   Jacobs, Z.: Composite grains from volcanic terranes: Internal dose rates of supposed 'potassium-rich' feldspar grains used

411   for optical dating at Liang Bua, Indonesia, Quat. Geochronol., 64, 101182, https://doi.org/10.1016/j.quageo.2021.101182,

412   2021.

Ostrooumov, M.: Amazonite, Elsevier, https://doi.org/10.1016/c2015-0-00152-6, 2016.

Phillips, D., Matchan, E., Gleadow, A., Brown, F., McDougall, I., Cerling, T., Leakey, M., Hergt, J., and Leakey, L.: 40Ar/39Ar eruption ages of Turkana Basin tuffs: millennial scale resolution constrains paleoclimate proxy tuning models and hominin fossil ages, J. Geol. Soc., 180, jgs2022-171, https://doi.org/10.1144/jgs2022-171, 2023.

Plummer, T. W., Oliver, J. S., Finestone, E. M., Ditchfield, P. W., Bishop, L. C., Blumenthal, S. A., Lemorini, C., Caricola, I., Bailey, S. E., Herries, A. I. R., Parkinson, J. A., Whitfield, E., Hertel, F., Kinyanjui, R. N., Vincent, T. H., Li, Y., Louys, J., Frost, S. R., Braun, D. R., Reeves, J. S., Early, E. D. G., Onyango, B., Lamela-Lopez, R., Forrest, F. L., He, H., Lane, T. P., Frouin, M., Nomade, S., Wilson, E. P., Bartilol, S. K., Rotich, N. K., and Potts, R.: Expanded geographic distribution and dietary strategies of the earliest Oldowan hominins and Paranthropus, Science, 379, 561–566, https://doi.org/10.1126/science.abo7452, 2023.

Prasad, A. K. and Jain, M.: Dynamics of the deep red Fe3+ photoluminescence emission in feldspar, J. Lumin, 196, 462–469, https://doi.org/10.1016/j.jlumin.2017.11.051, 2018.

Preusser, F., Degering, D., Fuchs, M., Hilgers, A., Kadereit, A., Klasen, N., Krbetschek, M. R., Richter, D., and Spencer, J. Q. G.: Luminescence dating: basics, methods and applications, Eiszeitalt. Ggw. Quat. Sci. J., 57, 95–149, https://doi.org/10.3285/eg.57.1-2.5, 2008.

Rasmussen, C. F., Christiansen, H. H., Buylaert, J.-P., Cunningham, A., Schneider, R., Knudsen, M. F., and Stevens, T.: High-resolution OSL dating of loess in Adventdalen, Svalbard: Late Holocene dust activity and permafrost development, Quat. Sci. Rev., 310, 108137, https://doi.org/10.1016/j.quascirev.2023.108137, 2023.

Ravel, B. and Newville, M.: ATHENA, ARTEMIS, HEPHAESTUS: data analysis for X-ray absorption spectroscopy using IFEFFIT, J Synchrotron Rad, 12, 537–541, https://doi.org/10.1107/S0909049505012719, 2005.

R Core Team: R: A language and environment for statistical computing. R Foundation for Statistical Computing, Vienna, Austria. URL https://www.R-project.org/, 2022.

Richter, D., Richter, A., and Dornich, K.: lexsyg — a new system for luminescence research, Geochronometria, 40, 220–228, https://doi.org/10.2478/s13386-013-0110-0, 2013.

Riedesel, S., Kumar, R., Duller, G. A. T., Roberts, H. M., Bell, A. M. T., and Jain, M.: Site-selective characterisation of electron trapping centres in relation to chemistry, structural state and mineral phases present in single crystal alkali feldspars, J. Phys. Appl. Phys., 54, 385107, https://doi.org/10.1088/1361-6463/ac10d7, 2021.

Sontag-González, M. and Fuchs, M.: Spectroscopic investigations of infrared-radiofluorescence (IR-RF) for equivalent dose estimation, Radiat. Meas., 153, 106733, https://doi.org/10.1016/j.radmeas.2022.106733, 2022.

Sontag-González, M., Li, B., O'Gorman, K., Sutikna, T., Jatmiko, Jacobs, Z., and Roberts, R. G.: Establishing a pIRIR procedure for De determination of composite mineral grains from volcanic terranes: A case study of sediments from Liang Bua, Indonesia, Quat. Geochronol., 65, 101181, https://doi.org/10.1016/j.quageo.2021.101181, 2021.

Sontag-González, M., Mittelstraß, D., Kreutzer, S., and Fuchs, M.: Wavelength calibration and spectral sensitivity correction of luminescence measurements for dosimetry applications: Method comparison tested on the IR-RF of K-feldspar, Radiat.

447   Meas., 159, 106876, https://doi.org/10.1016/j.radmeas.2022.106876, 2022.

448   Sontag-González, M., Kumar, R., Schwenninger, J.-L., Thieme, J., Kreutzer, S., and Frouin, M. Short communication:

449   Synchrotron-based elemental mapping of single grains to investigate variable infrared-radiofluorescence emissions [Dataset]

450   (v.1.0.0) [Data set]. Zenodo. https://doi.org/10.5281/zenodo.7971805, 2023.

451   Telfer, D. J. and Walker, G.: Ligand field bands of Mn^{2+} and Fe^{3+} luminescence centres and their site occupancy in

452   plagioclase feldspars, Mod. Geol., 6, 199–210, 1978.

453   Trautmann, T., Krbetschek, M. R., Dietrich, A., and Stolz, W.: Feldspar radioluminescence: a new dating method and its

454   physical background, J. Lumin., 85, 45–58, https://doi.org/10.1016/S0022-2313(99)00152-0, 1999a.

455   Trautmann, T., Dietrich, A., Stolz, W., and Krbetschek, M. R.: Radioluminescence Dating: A New Tool for Quaternary

456   Geology and Archaeology, Naturwissenschaften, 86, 441–444, https://doi.org/10.1007/s001140050649, 1999b.

457   Trautmann, T., Krbetschek, M. R., and Stolz, W.: A systematic study of the radioluminescence properties of single feldspar

458   grains, Radiat. Meas., 32, 685–690, https://doi.org/10.1016/S1350-4487(00)00077-9, 2000.

459   Varma, V., Biswas, R., and Singhvi, A.: Aspects of Infrared Radioluminescence dosimetry in K-feldspar, Geochronometria,

460   40, 266–273, https://doi.org/10.2478/s13386-013-0125-6, 2013.

461   Visocekas, R., Barthou, C., and Blanc, P.: Thermal quenching of far-red Fe^{3+} thermoluminescence of volcanic K-feldspars,

462   Radiat. Meas., 61, 52–73, https://doi.org/10.1016/j.radmeas.2013.11.002, 2014.

463
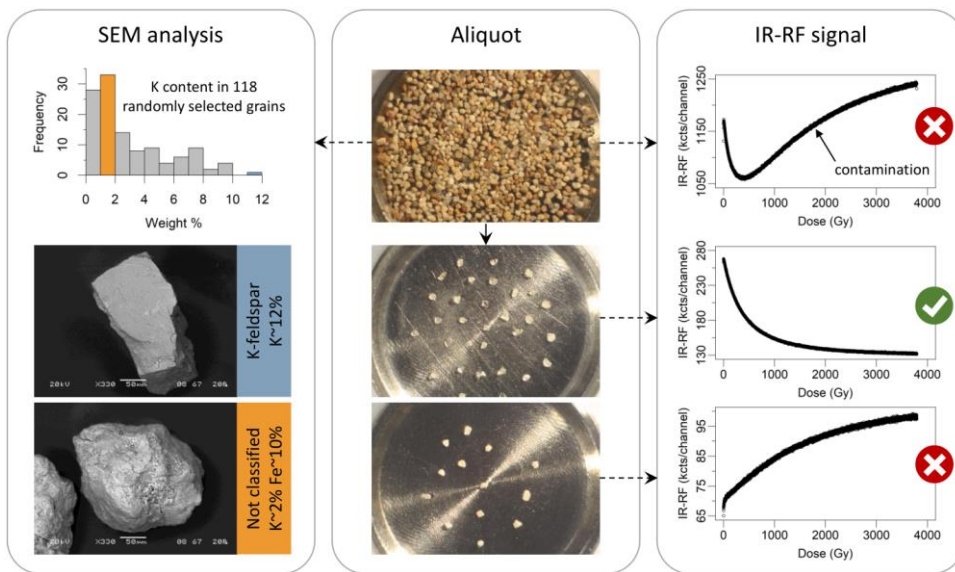
464 **Figure 1:** Illustration showing how contamination of the IR-RF signal can be removed by selecting only K-feldspar grains from sample

465 X7343. The regenerative IR-RF curves were obtained from aliquots containing hundreds of unsorted grains (top) or 10–30 grains manually

466 sorted into transparent shiny angular grains (middle) or white-pinkish rounded grains (bottom). The histogram shows the K-content

467 determined by SEM-EDS for 118 grains (not measured for IR-RF). Representative examples of grains classified as K-rich and contaminating

468 Fe-rich grains are shown.

469
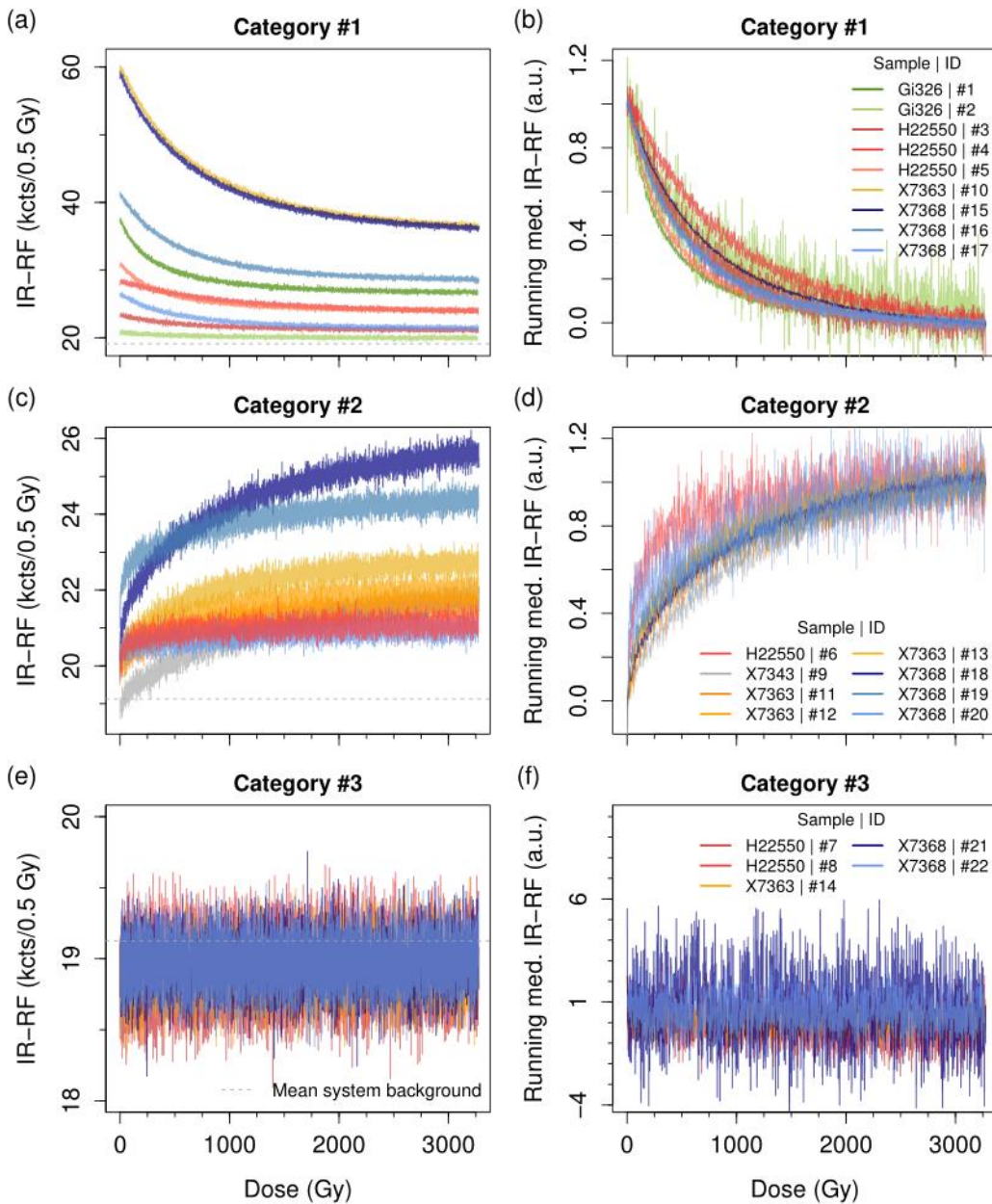
Figure 2: IR-RF dose-response curves of individual grains obtained after bleaching. Categories #1–#3 refer to grains with decreasing, increasing or no detectable signal, respectively (one category per row). The curves are shown (a, c, e) unnormalized and without background correction and (b, d, f) with intensities normalized to the signal maxima (defined as the median value of (b, f) the initial and (d) the final 20 channels) after subtracting as background the minimum signal of each grain (defined as the median value of (b, f) the final and (d) the initial 20 channels). For better visualisation, the normalized plots show the running median IR-RF with a window of 7 values. The system background was determined as the mean value obtained from measuring 5 empty cups under the same conditions as the grains.

476
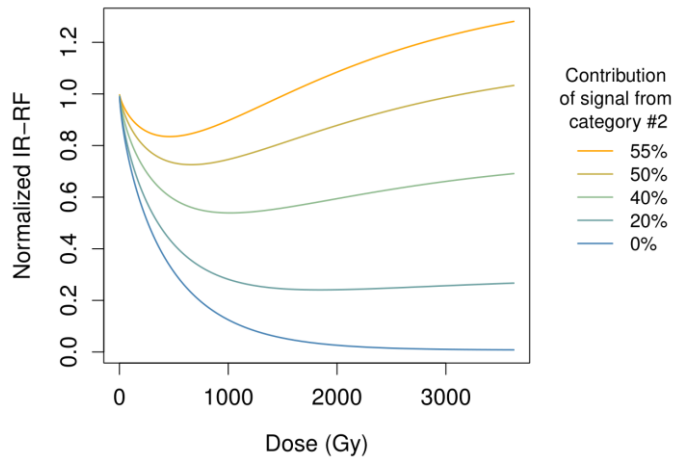
Figure 3: Simulated dose-response curves of theoretical aliquots varying the proportion of grains from categories #1 (desired decreasing
signal) and #2 (increasing signal). The curves are the sum of two stretched exponentials using parameters obtained from fits of grains from
samples Gi326 (category #1) and X3743 (category #2). The higher the signal contribution from category #2 grains, the more aberrant the
sum curve becomes.

481

482
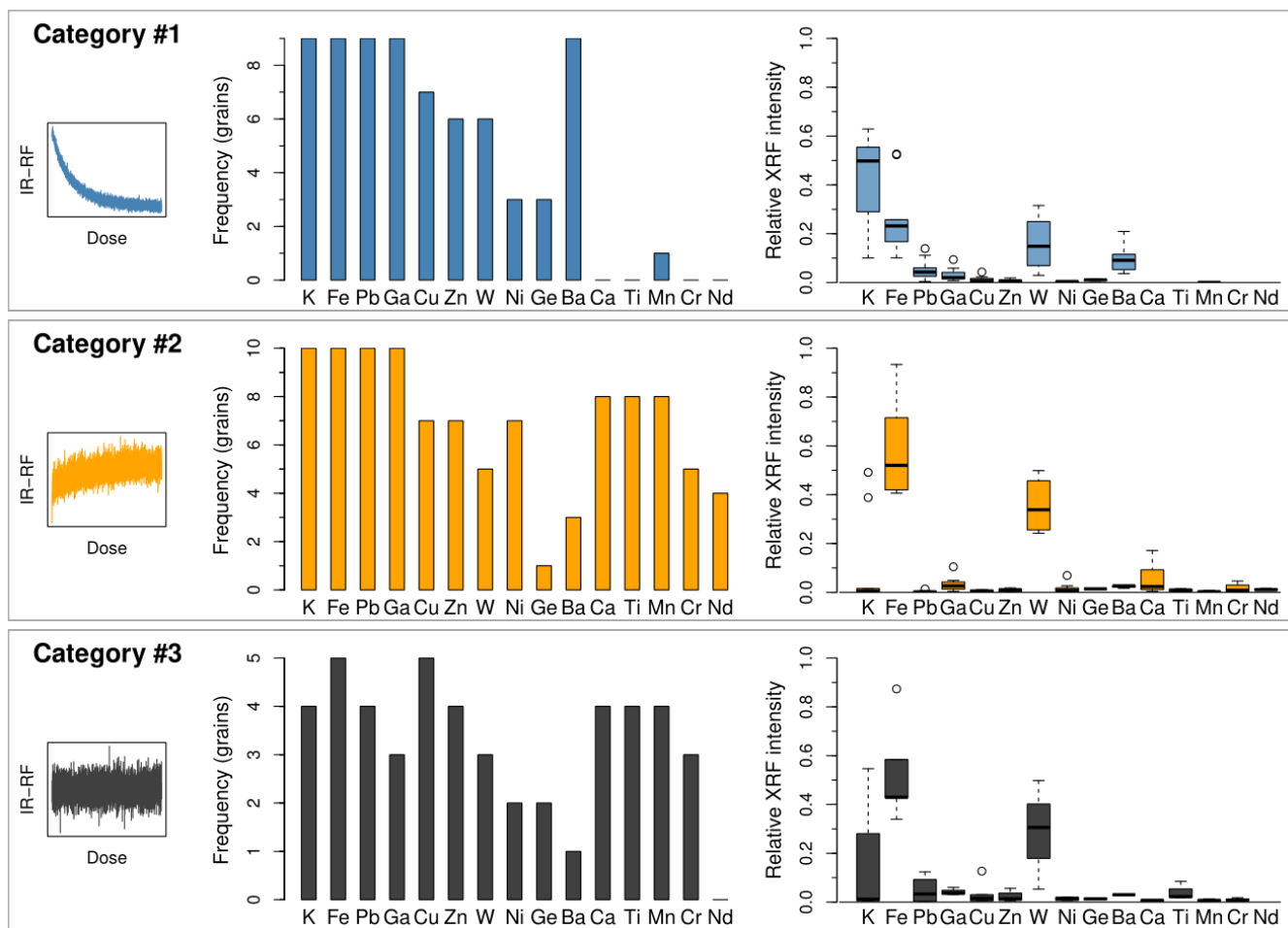
Figure 4: Bar charts of elements identified in µ-XRF spectra and boxplots of the relative µ-XRF intensities for grains in three categories, as exemplified in the insets: decreasing IR-RF signal (category #1), increasing IR-RF signal (category #2) or flat IR-RF signal indistinguishable from the background (category #3) during beta irradiation.

483
484
485
486
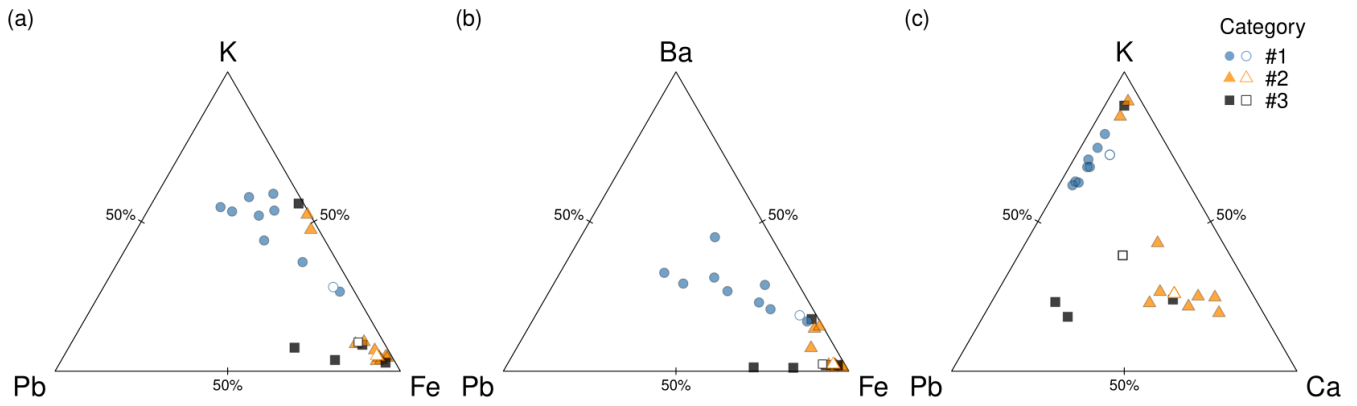
487
488 **Figure 5:** Ternary diagrams of relative μ-XRF intensities attributed to (a) K, Fe and Pb, (b) Ba, Fe and Pb, and (c) K, Ca and Pb for grains
489 of the three categories. Note that the contributions are not calibrated to mass or stoichiometry. The relative K contribution is, thus, not directly
490 comparable to the K-feldspar K-content. The three grains shown in figure 6 are marked as open symbols in each ternary diagram.
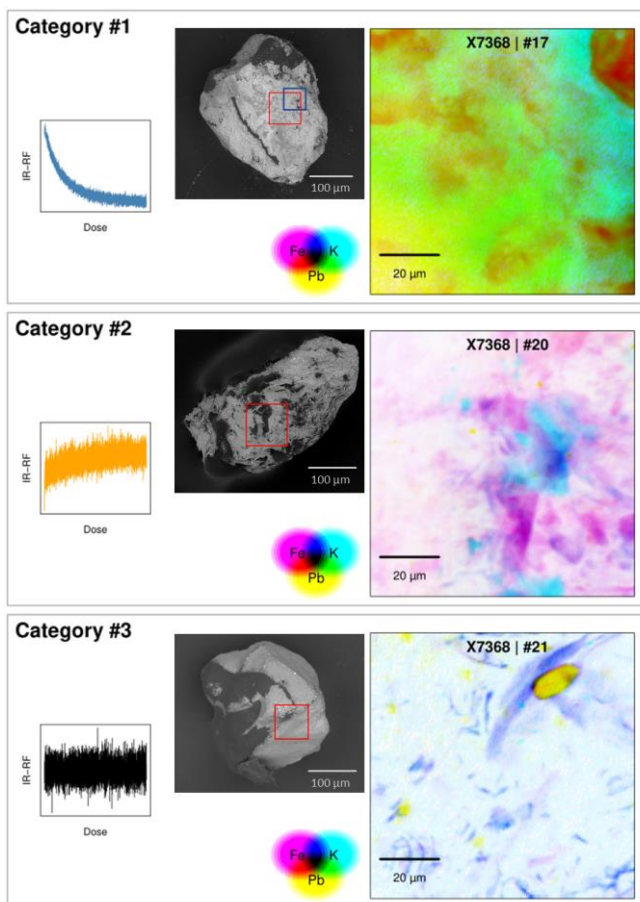
Figure 6: Illustration showing three IR-RF curves obtained from three grains of sample X7368, classified as follows: decreasing IR-RF signal (category #1), increasing IR-RF signal (category #2) or flat IR-RF signal indistinguishable from the background (category #3) during beta irradiation. μ-XRF spectra were measured from the area bordered by red squares on the SEM images of the grains. The maps show the presence of K, Fe, and Pb on the same grains as the IR-RF curves. The elemental compositions are shown overlaid, with the colour scales normalized to the maximum contribution of each element for each grain. The area bordered by a blue square in the category #1 grain corresponds to the map shown in figure 8.

498
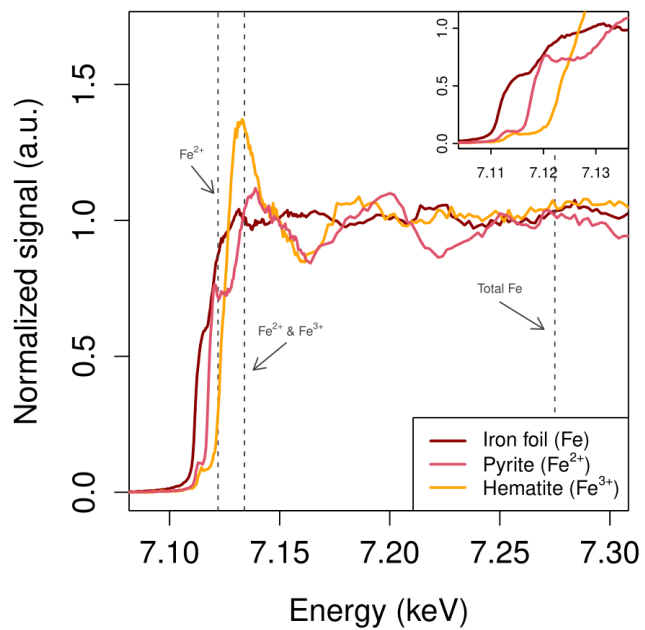
499 **Figure 7:** μ-XANES spectra of Fe standards. The dashed vertical lines indicate the incident beam energies necessary to isolate emissions

500 from specific oxidation states. The inset shows a magnification of the energy region relevant to determine the incident beam energies.

501

502
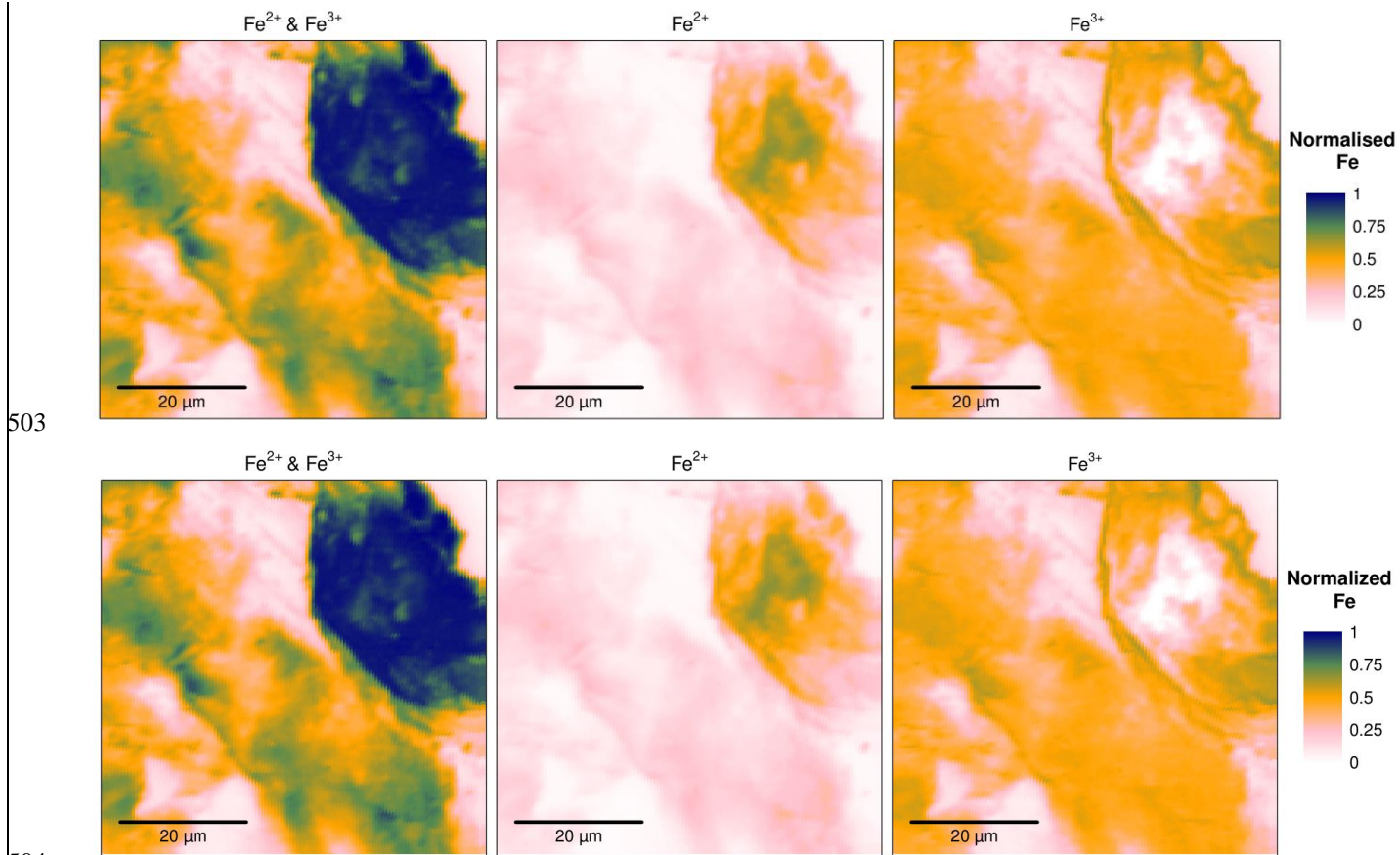
Figure 8: Maps of Fe oxidation states for a grain of sample X7368 (category #1; ID #17). Intensities are normalized to the maximum intensity of total Fe.

507 **Table1:** Overview of measured grains. Categories #1–#3 refer to grains with decreasing, increasing or no detectable signal, respectively.

508 For two grains, two regions each were mapped, so we measured a total of 24 µ-XRF maps.

Sample	Grain size (µm)	Number of measured grains		
		Category #1	Category #2	Category #3
Gi326	90–200	2	0	0
H22550	180–250	3	1*	2
X7343	180–255	0	1*	0
X7363	180–255	1	3	1
X7368	180–255	3	3	2
Total		9	8	5

509 *For these grains, two regions were mapped by µ-XRF: the grain 'matrix' and an inclusion.